

Fourier Transform Spectrometer Controller for Partitioned Architectures

D. Tămaş-Selicean¹, D. Keymeulen², D. Berisford², R. Carlson², K. Hand², P. Pop¹, W. Wadsworth³, R. Levy⁴

¹Technical University of Denmark, Anker Engelunds Vej 1, Kongens Lyngby, Denmark

²Jet Propulsion Laboratory, 4800 Oak Grove Drive, Pasadena, CA 91109

³Designs & Prototypes, Ltd, Nashua, NH 03060

⁴Quant Engineering, LLC, Doylestown, PA 18902

Abstract—The current trend in spacecraft computing is to integrate applications of different criticality levels on the same platform using no separation. This approach increases the complexity of the development, verification and integration processes, with an impact on the whole system life cycle. Researchers at ESA and NASA advocated for the use of partitioned architecture to reduce this complexity. Partitioned architectures rely on platform mechanisms to provide robust temporal and spatial separation between applications. Such architectures have been successfully implemented in several industries, such as avionics and automotive. In this paper we investigate the challenges of developing and the benefits of integrating a scientific instrument, namely a Fourier Transform Spectrometer, in such a partitioned architecture.

TABLE OF CONTENTS

D1. INTRODUCTION	1
2. FOURIER TRANSFORM SPECTROMETRY	2
3. COMPOSITIONAL INFRARED IMAGING SPECTROMETER (CIRIS)	3
4. CIRIS CONTROLLER IMPLEMENTATION	3
5. EVALUATION	7
6. PARTITIONED ARCHITECTURE	7
7. CONCLUSIONS	9
BIOGRAPHY	10
APPENDIX A: RUNNING SIGNAL-TO-NOISE RATIO (SNR)	11
ACKNOWLEDGEMENTS	11

1. INTRODUCTION

Spectroscopic techniques allow scientists to determine the composition of remote substances. Although there are numerous such techniques, most space-based spectrometers are dispersive spectrometers that measure the absorption of light in the near-infrared spectrum (wavelengths between 1 to 5 μm). Fourier Transform Infrared (FTIR) spectrometers are better suited for remote sensing, as they offer a considerable higher throughput (called the *Jacquinot* or throughput advantage) compared to the dispersive spectrometers [1], and also due to the mid-infrared range they operate in, which contains the fundamental vibrations for most of the relevant compounds.

The Fourier Transform Spectrometer (FTS) technique is based on the interference of light phenomenon. A beam splitter divides the polychromatic beam of light into two. One beam travels a fixed distance, while the other beam

travels a variable distance, depending on the position of a moving mirror. The beams recombine before hitting the detector. The detector records the intensity of the light for each position of the moving mirror, building an interferogram. This interferogram can be solved using a Fast Fourier Transform (FFT), thus obtaining the absorption spectrum. See Section 2 for a detailed description of the traditional FTS.

The current trend in spacecraft computing is to integrate applications of different criticality levels on the same computing platform, with little or no separation. Thus, all applications have to be developed and tested according to the processes defined by the highest criticality, increasing the complexity and cost of the system development and integration. This integrated approach affects the applications during the whole lifetime of the system, as a change to an application will affect the other applications, and this impact has to be thoroughly tested. This complexity increases furthermore if we consider that the applications can originate from different stakeholders.

In a recent paper [3], researchers from the European Space Agency (ESA) have advocated for the use of partitioned architectures (PAs) in spacecraft avionics, as a way to “manage the growth of mission functions implemented in the on-board software”. A similar case was made by researchers from the National Aeronautics and Space Administration (NASA) [12]. As the number of missions carrying payloads from different stakeholders increases, work is done to ensure that partitioning protects applications from each other in the safety domain, as well as in the security domain [13]. Furthermore, ESA views PAs as an intermediate step to introducing multi-core processors in spacecraft computers [13].

Partitioned architectures rely on partitioning mechanisms at the platform level to ensure temporal and spatial separation between applications of different criticality levels, and thus to allow the safe integration on the same platform. As pointed out in [2], implementing the Phobos I spacecraft using a partitioned architecture would have prevented its loss, as the flight critical software would have been protected from the failures of other applications, in this case, a keyboard buffer overflow. Such architectures have been successfully used in several industries, including automotive and avionics. For example, in the avionics area, platform level separation mechanisms are described in the ARINC 653 software specification, also called “Integrated Modular Avionics” [2].

Spatial partitioning protects the private data or devices of an application in a partition from being tampered with, by another application. It usually relies on hardware mechanisms such as Memory Management Units (MMUs). Alternatives were proposed for spatial partitioning in spacecraft processors that do not have MMUs [10]. A detailed discussion on partitioning can be found in [2].

With PAs, each application is running in its own partition. On a processor, a partition is defined as a sequence of partition slices. A partition slice is a predetermined time interval in which the application is allowed to use the CPU. A static partition table specifies the sequence and length of partition slices on a CPU. Temporal partitioning ensures that an application's access to shared resources is not affected by applications in other partitions. As a consequence, partitions can implement different scheduling policies. Moreover, each partition could host its own operating system.

To name just a few of the advantages of using partitioned architectures for spacecraft platforms, PAs allow the safe and secure integration of applications of different criticality levels and from different stakeholders on the same platform, by providing a robust fault containment. Such a platform reduces the development, verification and integration efforts, and thus the associated costs. PAs are proven in use in the avionics and automotive industries. A detailed discussion on the benefits of Integrated Modular Avionics (IMA) for spacecraft can be found in [11, 12].

In this paper we develop a hard real-time application and investigate the benefits of integrating it on a PA-like platform. The application in question is the controller for a FTIR spectrometer. The instrument under development at the Jet Propulsion Laboratory is the Compositional InfraRed Imaging Spectrometer (CIRIS), based on the TurboFT [5] spectrometer design, which was developed by Designs and Prototypes, Ltd., under a contract for the US Army Edgewood Chemical and Biological Center, and with the Commonwealth Scientific and Industrial Research Organisation in Australia. Anderson et al. [8] propose a similar FTIR instrument based on the TurboFT spectrometer that can be used for Mars missions, as well as in Antarctic field studies. A similar concept to the TurboFT instrument was developed for a spectrometer onboard the European Mars Express mission [7]. In our configuration, the hard-real time requirements of the instrument is to acquire a 8192 points interferogram over a period of 33 ms every 100 ms.

The paper is organized as follows: Section 2 describes the traditional Michelson spectrometer. Section 3 presents the CIRIS instrument. The controller for this instrument is detailed in Section 4, followed by the experimental results presented in Section 5. Section 6 presents reasons and implications of implementing the CIRIS controller on a partitioned architecture.

2. FOURIER TRANSFORM SPECTROMETRY

The schematic of a traditional Michelson FTIR spectrometer is shown in Figure 1. The basic configuration is comprised of a beam splitter and two mirrors, with the plane of the fixed mirror M_f perpendicular on the plane of the moving mirror M_m . As the beam of light passes through the beam splitter, it is divided into two separate beams, b_1 and b_2 . The reflected beam b_1 travels a fixed distance. The transmitted beam b_2 is reflected by the moving mirror M_m , and thus travels a variable distance, depending on the position of M_m . The beams recombine at the beam splitter and the intensity of the recombined beam b_r is detected by the Detector.

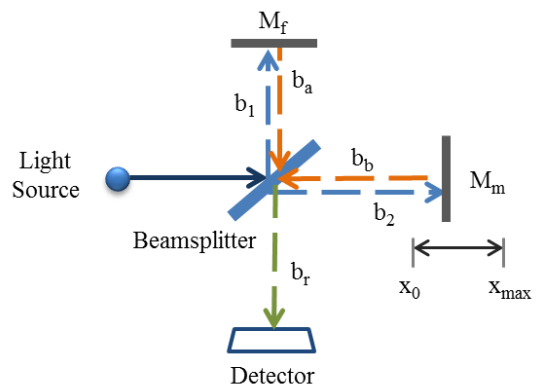


Figure 1 Basic Michelson interferometer

M_m moves in a linear trajectory between positions x_0 and x_{max} . When M_m is in the x_0 position, the distance travelled by beams b_1 and b_2 are equal. In this case, the *optical path difference* (OPD) between the two beams, that is the difference in the distance travelled by the beams, is zero. Consequently, constructive interference occurs as the two beams recombine at the beam splitter, and the intensity of the recombined beam b_r at the detector is maximized.

As the mirror M_m linearly moves away from the x_0 position, the OPD increases and a *phase shift* is introduced between the two beams. Thus, at each position of M_m , the recombined beam contains a different combination of wavelengths, and its intensity varies. The recorded intensity of the recombined beam, as a function of the OPD is called an *interferogram*. By processing the interferogram using a Fast Fourier Transform (FFT), we obtain the spectrum of the input beam, as the intensity of each wavelength.

According to the Rayleigh criterion [4], the resolution $\Delta(\nu)$ of the spectrometer is determined by the maximum motion of the moving mirror (which in turn determines the OPD):

$$\Delta(\nu) = 1/\max(OPD) \quad (1)$$

The reader is directed to [1, 4] for more details on the subject of Fourier Transform spectroscopy instrumentation and engineering.

3. COMPOSITIONAL INFRARED IMAGING SPECTROMETER (CIRIS)

In the case of the CIRIS instrument (see Figure 2), the OPD between the two beams is modified using a rotating refractor, instead of a linear moving mirror like in the traditional Michelson FTS. The refractor spins at a constant velocity, thus the OPD can be easily determined for each refractor angle. The OPD is zero when the refractor's plane is parallel or perpendicular on the beam splitter, that is, both beams travel at an angle of 45° through the refractor, and thus both beams travel the same length. The OPD has a maximum value when the refractor is perpendicular on one of the beams, and thus, one beam's path is maximized, while the other one's is minimized. Since during each revolution the refractor has four positions with zero OPD (ZPD), each complete refractor revolution yields 4 interferograms.

The linear motion system of the Michelson interferometer presented in Section 2 is very sensitive to vibrations and non-linear errors. An incorrect angle of the moving mirror causes optical path length errors [1], affecting the quality of the output spectra. Moreover, a monochromatic reference laser is usually used as a sampling clock signal, adding to the complexity of the spectrometer and can lead to data sampling errors.

The rotating refractor design of the CIRIS instrument increases the robustness of the FTS, reducing the alignment errors. Furthermore, this design eliminates the need for a reference laser, as the position of the refractor can be accurately reported using an optical encoder mounted on the DC servomotor controlling the refractor. The TurboFT spectrometer, on which CIRIS bases its design, was tested aboard helicopters for remote sensing applications in Australia, confirming the ruggedness of this design [5].

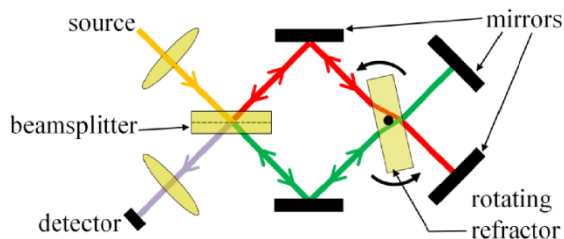


Figure 2 CIRIS interferometer

To obtain a non-distorted interferogram, the light is acquired in the optical region where the OPD is a linear relation with the angle of the refractor. The linear region corresponds to a scan angle limited to ± 15 degrees around the ZPD position [5] and a duty cycle of 33%. The rotation speed of the refractor is limited by frequency bandwidth (50kHz) of a very low noise ($1fA/\sqrt{Hz}$) high gain (10^8) transimpedance preamplifier needed to observe icy moons. In summary, the TurboFT spectrometer has an angular speed of 2.5

revolutions per second, and a single interferogram is captured during 33 ms every 100 ms.

The CIRIS instrument is operational in the spectral range of 2.8 to 18 μm , or 3571 to 555 cm^{-1} . The 4 cm^{-1} resolution is limited by the aperture of the instrument and the refractor thickness, while the optical bandwidth is limited by the scan angle and choice of detectors. The FTS spectra has a resolution of 754 points between 3571 and 555 cm^{-1} (2.8 and 18 μm). The spectra can be computed from a single sided interferogram with 1508 points or from a double sided interferogram (insensitive to phase change), with at least 3016 points. While 4096 interferograms points acquired over 33 ms will be sufficient, our CIRIS implementation records 8192 interferograms data points for each interferogram. As a consequence, we add more data points at the shortwavelength of the spectrum, while the interesting part of the spectrum is further away from the Nyquist frequency, compared to the spectrum obtained from 4096 points. This improves the anti-aliasing of the signal. Considering that the scan period is of 33 ms, the sampling frequency is set to 4 μs per interferogram data point.

More details on the spectrometer can be found in [5]. Researchers presented in [6] the testing results of the prototype, together with several detectors.

4. CIRIS CONTROLLER IMPLEMENTATION

Considering the hard real-time requirements of the CIRIS instruments presented in the previous Section, as well as the environment it will operate in, we choose to implement the controller on a CompactRIO (cRIO) platform from National Instruments (NI). cRIO is a "small rugged control and acquisition system" [9] for industrial use. A cRIO platform is composed of a cRIO 9025 controller module processor running a real-time operating system (RTOS), a back-plane cRIO 9118 with a reconfigurable, user-programmable FPGA and hot-swappable I/O modules such as NI 9223 with 4 ADC channels 16-Bit 1MSamples/second and NI 9263 4-Channel DAC 16-Bit 100kSamples/second.

The proposed scenario is that the controller is partially implemented on the FPGA board, and partially on the spacecraft computer. As such, the RTOS-running processor is simulating the spacecraft computer, which is shared by application of different criticality levels.

We implemented the CIRIS controller on a cRIO 9025 rugged controller, which contains an 800 MHz PowerPC processor running the VxWorks RTOS from WindRiver. The chassis is a NI 9118 Reconfigurable Embedded Chassis, containing a Xilinx Virtex-5 LX110 reconfigurable FPGA core, which executes at a default rate of 40 MHz.

Figure 3 presents the schematic of our CIRIS setup, while Figure 4 shows a photo of the physical setup in the lab. The cRIO 9025 controller is depicted in the figure with "RT

Host” box, while the NI 9118 chassis is represented by the “FPGA” box. The Motor Control Unit (MCU) controls the velocity of the rotating refractor using the output signals of the optical encoder and is currently running in a full independent analog loop.

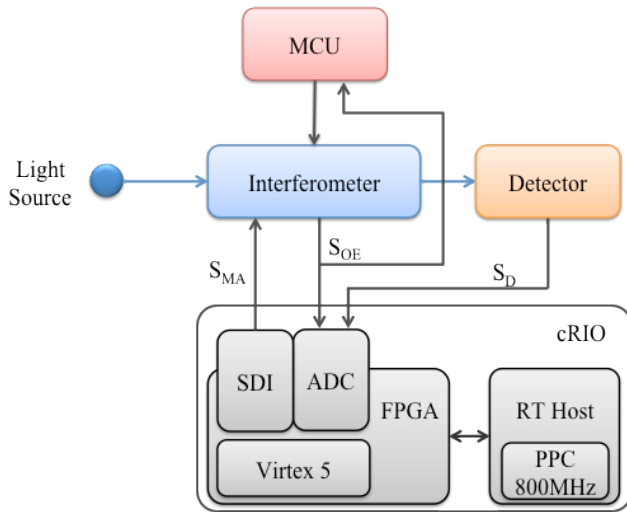


Figure 3 CIRIS setup schematic

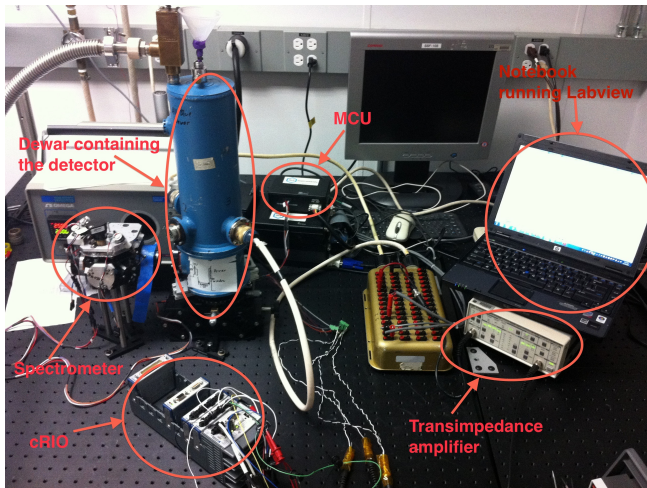


Figure 4 Physical setup of the CIRIS Instrument

In order to meet the hard real-time requirement of reading an interferogram data point every $4 \mu\text{s}$, we use a NI 9223 Simultaneous Analog Input module (depicted with ADC in Figure 3) to convert the detector signal S_D reading. The NI 9223 is capable of simultaneously reading from its 4 channels, at a rate of 1 MSamples per second, or 1 sample per μs , making it highly suitable for our application.

The correctness of the resulted spectrum depends not only on the noise of each point of the interferograms, but also on the proper data sampling of the interferogram. We use the angle of the rotating refractor to determine the sampling. In the CIRIS instrument, the angle of the refractor is signaled by a FAULHABER E2-360I [17] optical incremental encoder mounted on the DC servomotor controlling the

rotating refractor. The E2-360I optical encoder completes 360 cycles during a revolution. It employs three outputs: Channel A and Channel B, with 90° phase shift, encode the logic state of the cycle, while Channel Index signals the completion of a revolution. Figure 5 presents the logic states of the output channels. These optical encoder signals S_{OE} are converted by the ADC and used as inputs in our application.

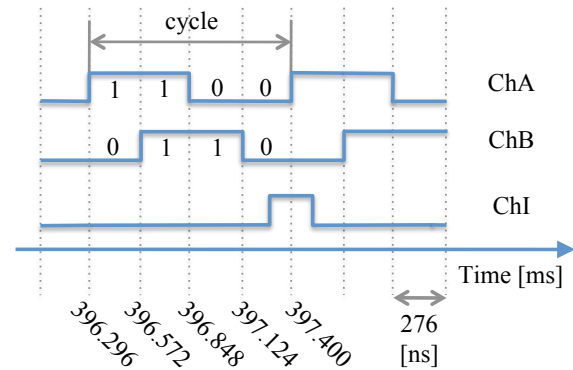


Figure 5 Optical encoder output channels logic states.

Due to external forces, mirror misalignment may occur during the lifetime of operation, affecting the quality of the resulting interferograms. Alignment correction is performed using the 4 mirrors of the interferometer. A NI 9512 Stepper Drive Interface (SDI) Module, depicted in Figure 3, controls the stepper motor linear actuators connected to each mirror, through the mirror alignment signal S_{MA} . The optical alignment is achieved by maximizing the power at the detector for a zero path delay configuration of the refractor.

Figure 6 presents the high-level description of our acquisition and processing controller algorithm. This algorithm is partly implemented on the FPGA, and partly on the Real-Time Host (RT Host). We mark the number of the algorithm steps in green circles. In the first step, the controller identifies the rotating refractor position (1), by using the optical encoder signals from channels A, B and I, respectively. In case the refractor is at -15 degree from ZPD of one of the 4 rotational positions, the controller starts sampling for 8192 data points. The read data is filtered (3) using a bandpass filter between 3 and 100 kHz. After the ZPD position is identified (4), the interferogram can be zero-centered (5). Steps 1 to 5 compose the Interferogram Acquisition Process (IAP). The centered interferogram is Fast Fourier Transformed (6), resulting in a raw spectrum. This spectrum is handed over to the RT Host, where it is further processed separately for each rotational position, with rotational position dependant coefficients. For each of the rotational positions (7), the spectra are averaged per position (8), dispersion corrected in the wave number domain (9) and the amplitude of the spectra is calibrated to spectral radiance in $\text{W}/(\text{m}^2 \times \mu\text{m})$ (11). Finally, the average of the resulting spectra is computed (13). These steps are described in greater detail below.

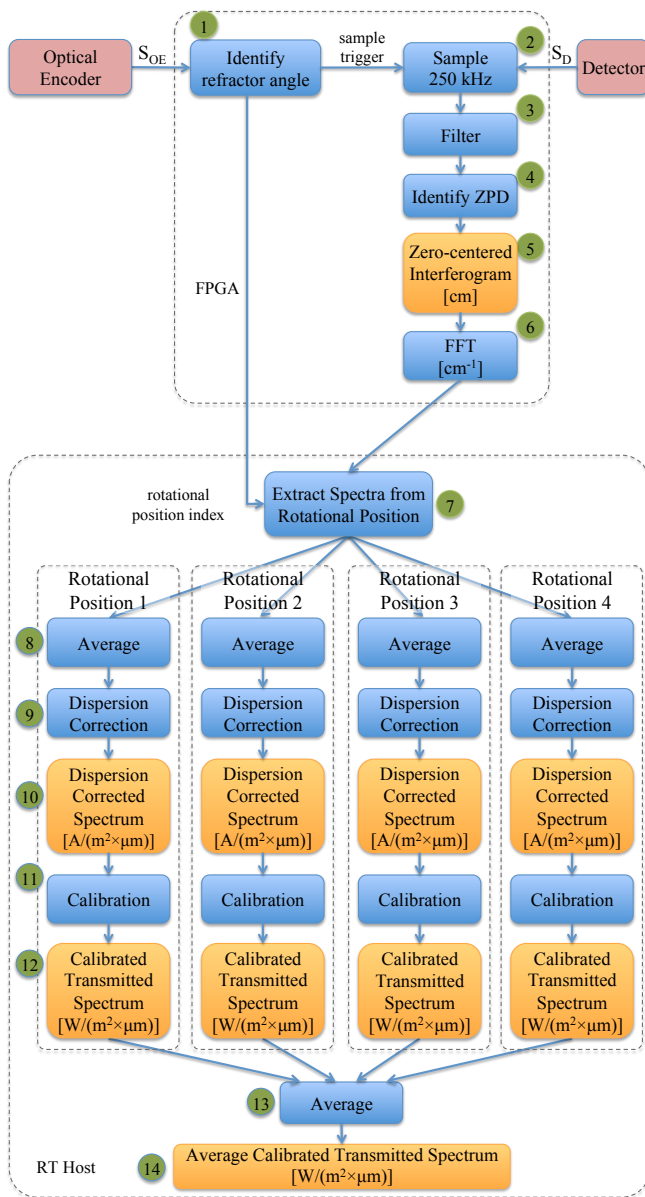


Figure 6 CIRIS high-level acquisition and processing algorithm description

Interferogram Acquisition

The interferogram acquisition process uses the optical encoder outputs Channel A and Channel B (ChA ChB) to identify the angle of rotating refractor. ChA ChB output signals each have 360 cycles per revolution, and they generate 1440 states per revolution. Figure 5 presents the logic states of the output channels. Each state corresponds to a turn of 0.25° angle of the rotating refractor. An interferogram covering approximately 30° spans over 120 ChA ChB states. Once the IAP identifies that the current ChA ChB logic state corresponds to the first logic state of the 120 covered by an interferogram (step 1 in Figure 6), it starts sampling (step 2 in Figure 6) for 8192 points. It samples using an FPGA hardware clock with a frequency of 250 kHz. The Channel I encoder output signals the complete

turn of the refractor, and triggers the reset of the sampling counters.

The read data is filtered using a band pass filter between 3kHz and 100 kHz (step 3 in Figure 6). As a state of the encoder covers around 69 samples (we are sampling the interferogram for 8192 points over 120 logic state numbers) and to get the double interferogram as symmetric as possible, the IAP centers the ZPD of the interferogram before performing the Fast Fourier Transform. This is done first by identifying the ZPD (step 4 in Figure 6) in the filtered data and then choosing 8192 points around the ZPD to obtain a centered interferogram (5), ready for the FFT (step 6 in Figure 6). Figure 7 presents the ZPD centered interferogram reading at rotational position 1.

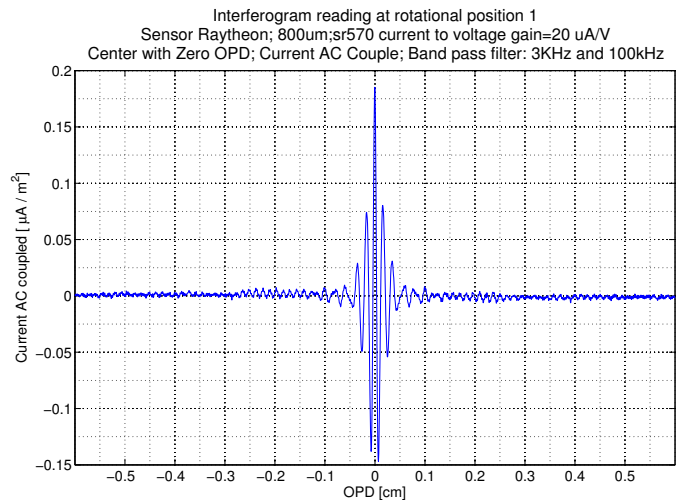


Figure 7 Interferogram reading at rotational position 1

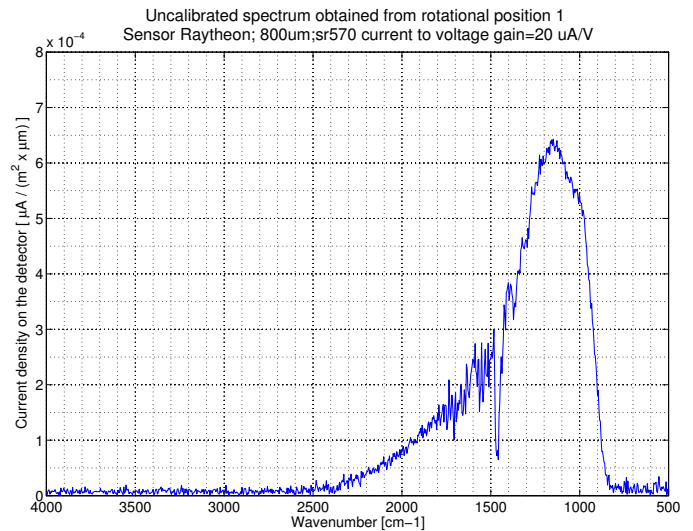


Figure 8 Uncalibrated spectrum obtained from rotational position 1

Position—dependant processing

Figure 8 presents the uncalibrated spectrum obtained after the FFT of the interferogram in Figure 7. The spectra obtained after the FFT on the FPGA (step 6 in Figure 6), are

further processed on the RT Host, which has a dedicated floating point unit. This processing is refractor position specific, as the path delay of the beam is not exactly the same for each refractor position (see Figure 2). Figure 9 shows there are differences between the spectra obtained at different rotational positions, by using the running signal to noise ratio (SNR), with an interval of 50 points (see Appendix A for more details on the computation of the running SNR). As such, the controller averages the resulted spectra, per each rotational position (step 8 in Figure 6) and processes the averaged spectra with position specific coefficients.

The *dispersion correction* process (step 9 in Figure 6) improves the wavenumber scale generated by the FFT, taking into consideration the rotational position of the spectra. The correction is an offset in wavenumbers (cm^{-1}), to the linear scale generated from the FFT. The form of the offset:

$$X_{corrected} = X_{fft} + c + 10^{m \times X_{fft} + b} \quad (2)$$

For ZnSe optics, $m = 0.000172$ and $b = 0.993$, while c is rotational position specific, and can be easily obtained by comparing the CIRIS spectra for each rotational position with a reference spectrum.

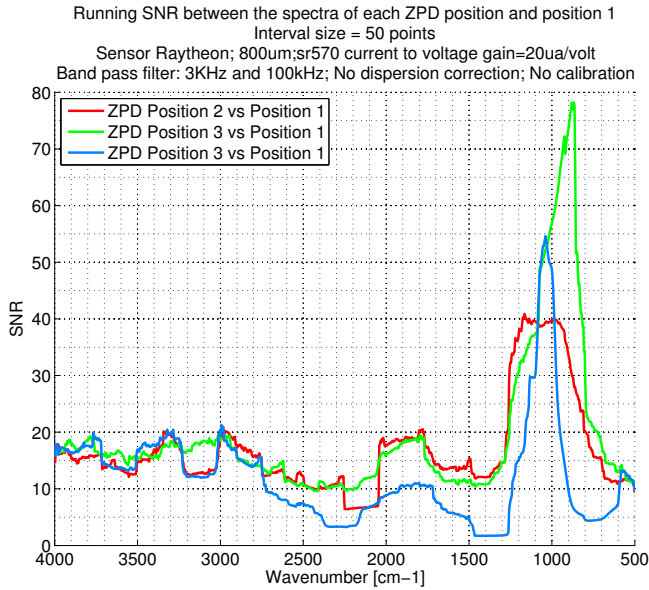


Figure 9 Running SNR comparison between the spectra at different ZPD positions

Amplitude Calibration

In order to provide consistent results over different measurements, the spectral amplitude has to be calibrated. This is done by reading the spectra corresponding to a blackbody at low and high temperature T_L and T_H , respectively, for each rotational position. We denote with $S(T, \nu)$ the measured spectrum of the blackbody at

temperature T in function of the wavenumber ν . Next, we compute the theoretical spectral radiance corresponding to the two temperatures, using Planck's law. We denote with $B(T, \nu)$ the spectral radiance at the surface of the blackbody at the temperature T for wavenumber ν . For the measured spectrum $S(T, \nu)$, we compute the calibrated reading $T_{Calibrated}$ using the equation below:

$$T_{Calibrated}(T, \nu) = \frac{S(T, \nu) - S(T_H, \nu)}{S(T_L, \nu) - S(T_H, \nu)} \times (B(T_L, \nu) - B(T_H, \nu)) + B(T_H, \nu) \quad (3)$$

This equation can be rewritten as:

$$T_{Calibrated}(T, \nu) = S(T, \nu) \times \frac{1}{Responsivity(\nu)} + Offset(\nu) \quad (4)$$

with the responsivity of the detector $Responsivity(\nu)$ and $Offset(\nu)$:

$$Responsivity(\nu) = \frac{S(T_L, \nu) - S(T_H, \nu)}{B(T_L, \nu) - B(T_H, \nu)} \quad (5)$$

$$Offset(\nu) = S(T_H, \nu) \times \frac{B(T_L, \nu) - B(T_H, \nu)}{S(T_L, \nu) - S(T_H, \nu)} + B(T_H, \nu) \quad (6)$$

The values for $Responsivity$ and $Offset$ are computed a priori of performing the calibration presented in step 11 in Figure 6. Figure 10 presents the detector responsivity computed using $T_L = 338.7\text{K}$ and $T_H = 422\text{K}$.

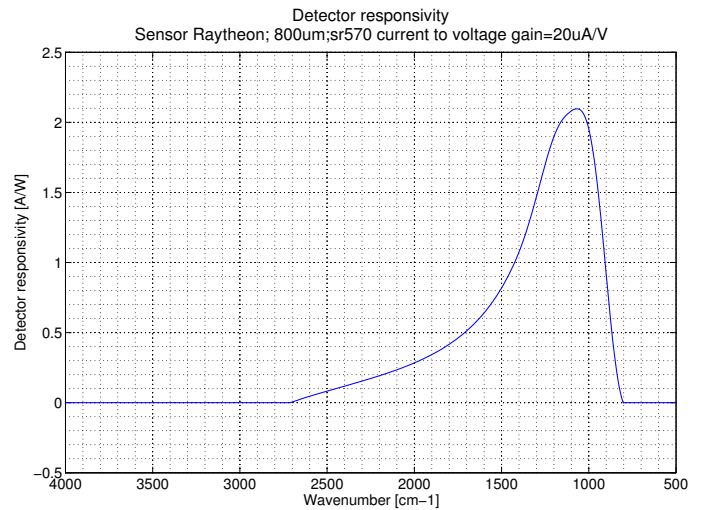


Figure 10 Detector responsivity

Transmittance and Absorbance

The calibrated transmitted spectrum (step 14 in Figure 6) is obtained by averaging the calibrated spectra (step 12) over the four rotational positions (step 13 in Figure 6). The transmittance $T(\nu)$ of a sample at wavenumber ν is measured by computing the ratio of the sample transmitted spectrum $T_{\text{Sample}}(\nu)$ over the background transmitted spectrum $T_{\text{Background}}(\nu)$. The background spectrum is obtained by measuring the spectrum without sample.

$$T(\nu) = \frac{T_{\text{sample}}(\nu)}{T_{\text{background}}(\nu)} \quad (7)$$

The absorbance of $A(\nu)$ of a sample at wavenumber ν is computed using the equation below.

$$A(\nu) = -\log_{10}(T(\nu)) \quad (8)$$

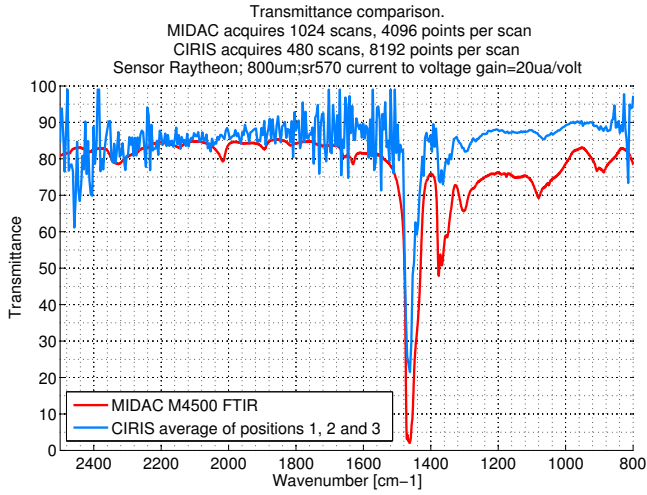


Figure 11 Transmittance comparison between the results obtained with CIRIS and MIDAC M4500 FTIR

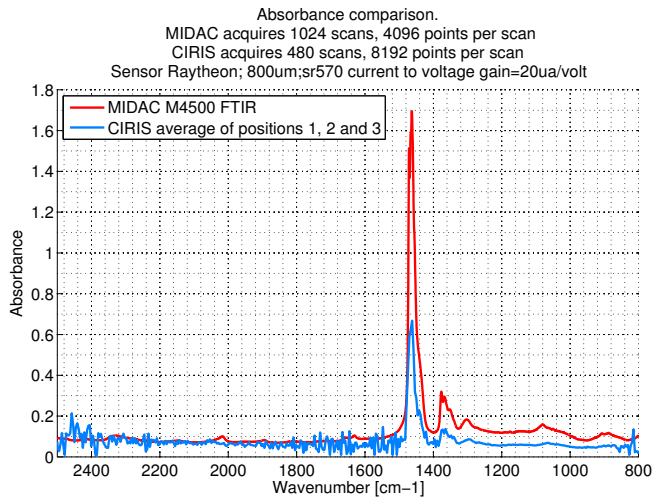


Figure 12 Absorbance comparison between the results obtained with CIRIS and MIDAC M4500 FTIR

5. EVALUATION

We evaluate the quality of our implementation by comparing the results from the CIRIS instrument with the results obtained from a MIDAC M4500 FTIR spectrometer. The MIDAC spectrometer uses ZnSe optics with HgCdTe detector. It has a resolution of 4 cm^{-1} , covering wavenumbers from 6000 to 600 cm^{-1} .

Figure 11 and Figure 12 present the transmittance and absorbance, respectively, of a plastic sample obtained respectively with the CIRIS instrument and with the Michelson-based FTIR instrument (MIDAC M4500). The spectral features are similar. The MIDAC absorbance is smoother due to the differences in data acquisition and processing: the MIDAC instrument acquires 4096 points per interferogram and average over 1024 spectra, while the CIRIS instrument acquired 8192 points per interferogram and average over 480 spectra. In addition, the MIDAC spectrometer performs triangle apodization of the interferogram [1], and Mertz phase correction [18]. The difference in the amplitude of the absorbance peak between the two instruments is attributed to the black body calibration of the CIRIS instrument and the different experimental setup of the CIRIS instrument compared to the MIDAC.

6. PARTITIONED ARCHITECTURE

The proposed implementation scenario is that the real-time Host computer shares its resources with applications of different criticality levels. In case this architecture is not partitioned, all applications need to be developed and certified according to the same standards and processes as the applications with the highest criticality level. This will increase the development and integration costs of the CIRIS instrument. The integration of the controller for the CIRIS instrument on an unpartitioned architecture will affect the signal to noise performance of the instrument, as the real-time requirements may not be met.

In the current setup, the motor control unit (MCU) is considered as a separate application, implemented on an analog board. Figure 13 presents the rotating refractor angular velocity measured by the duration between two logic codes defined by a ChA ChB. Figure 14 presents the angular velocity variation, relative to the duration of a complete revolution, as reported by ChI. Figure 15 reports the velocity variation measured between two consecutive ZPD peaks. Table 1 summarizes the results in Figure 13, Figure 14 and Figure 15, respectively, and shows the mean and the standard deviation of the refractor velocity measured at 3600Hz using ChA ChB signals, at 2.5 Hz using the ChI signal and at 10Hz using the ZPD.

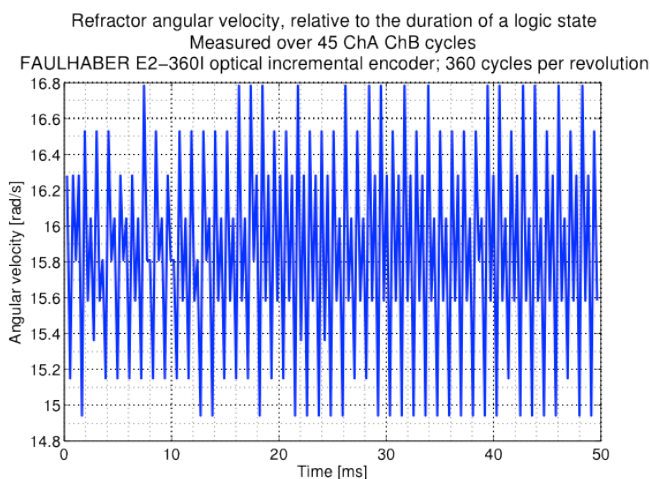


Figure 13 Angular velocity variation, relative to the duration of a ChA ChB logic state

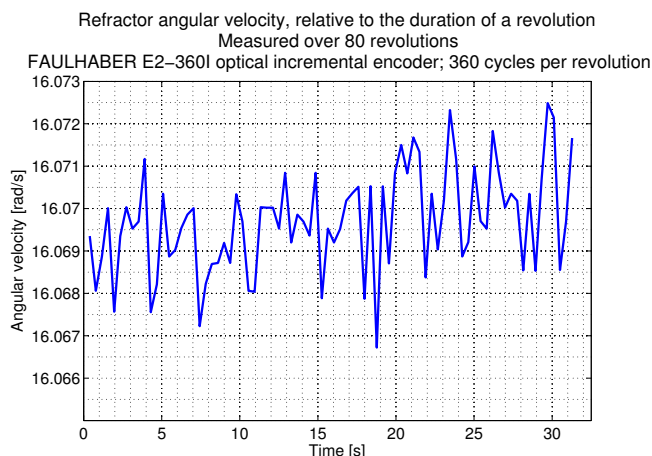


Figure 14 Angular velocity variation, relative to the duration of a revolution, as reported by ChI

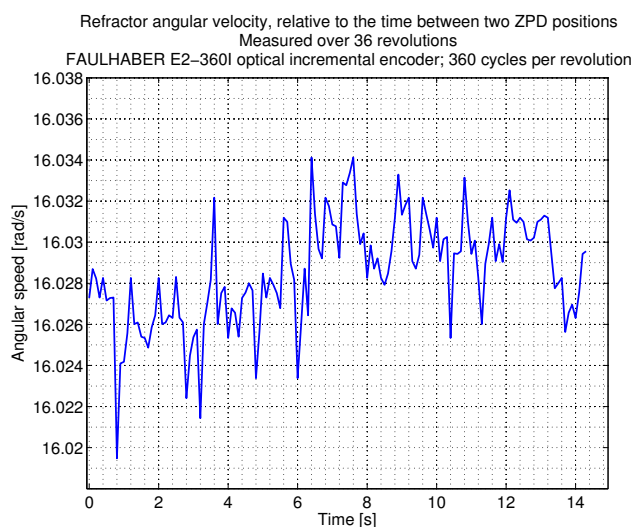


Figure 15 Angular velocity variation, relative to the duration of a revolution, as reported by the ZPD for each rotational position

Table 1 Rotating refractor velocity mean and standard deviation

Frequency [Hz]	Mean velocity [rad/s]	Standard deviation [rad/s]
3600	15.834	0.606000
10	16.028	0.003611
4	16.069	0.001211

As shown in Table 2, the encoder signals ChA and ChB measure accurately the mechanical position of the refractor. The table presents the ChA ChB logic state number for each of the four ZPD positions over 40 revolutions. Each of the four ZPD positions are located at the same logic state number. Figure 16 below shows what may happen if in place of implementing the MCU on an unpartitioned platform (single analog board), the velocity control is implemented on a process on the RT host sharing together resources with the other applications. It will result in a much more noisy control of the refractor velocity, affecting the quality of the spectra. Figure 16 was obtained by simulating the velocity noise as a sinusoidal function with a frequency of 600 cycles/cm mirror travel, injected in the sampling of the interferogram data points. We used the methodology presented in Appendix C of [1].

Table 2 Logic state numbers of the ZPD positions

ZPD position	Mean value of ChA ChB logic state number	Standard deviation
1	233	0
2	595	0
3	956	0
4	1315	0

The signal to noise performance of the instrument is degraded also if the real-time requirements of the controller are not achieved imposing that the measurements have to be interrupted to handle other applications with highest priority. For example, let us assume the CIRIS spectrometer is aboard a satellite making spectral measurements of a particular spot on the surface of an icy moon. In this case, the instrument will need to take continuous measurements of the same spot for a number of scans to increase the SNR. Moreover, these measurements will need to be continuously processed. A usual number of required scans to average is in the range of a several hundreds, thus the interferogram acquisition and processing spans over tens of seconds. When the applications handling the acquisition and processing of the spectra share the computing resource, there are situations when mission-critical applications (navigation and power management) might unnecessarily monopolize the CPU, preventing the CIRIS controller from executing. In this case, the number of processed spectra will be reduced, severely affecting the signal to noise of the resulting spectra.

Moving SNR of the spectrum affected by sinusoidal sampling noise
Increase in the amplitude of the noise

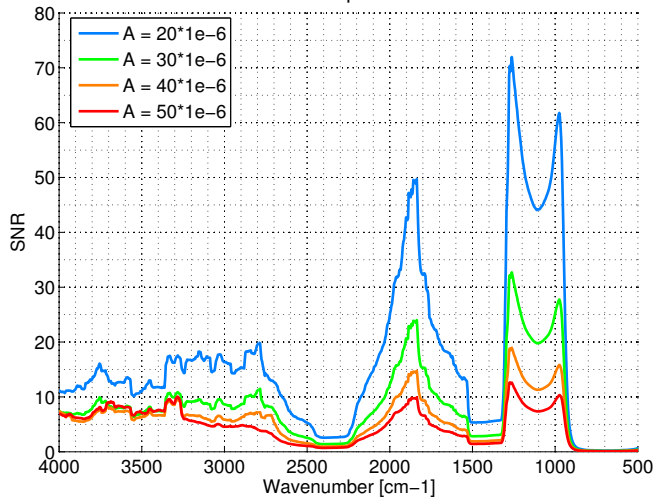


Figure 16 Impact of increasing refractor velocity noise on the spectra moving SNR

Figure 17 shows the impact of the number of spectral scans used during averaging processed over the SNR of the final spectrum. We compute the running SNR with an interval size of 50 points. This figure shows that reducing the number of spectral scans by 32 reduces the SNR of the final spectrum by 6, as expected for white noise.

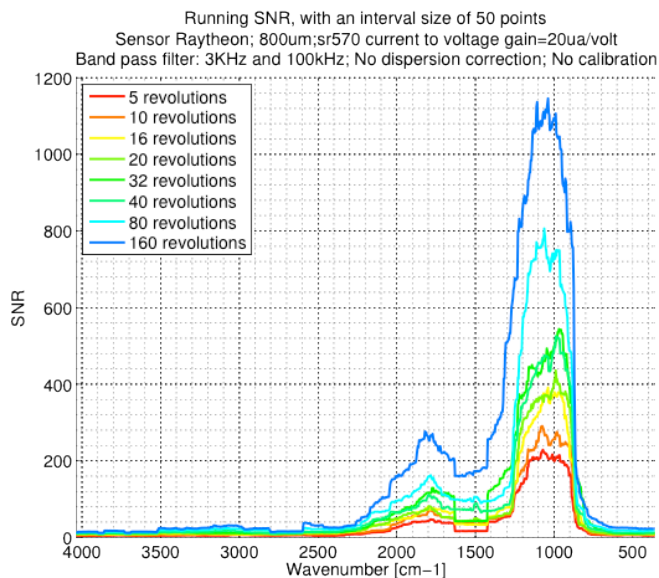


Figure 17 Comparison of running SNR of an interval size of 50 points, over different number of revolutions

A partitioned architecture implements robust spatial and temporal separation between applications. At the RT Host level, a partitioned operating system guarantees that each application will execute according to an offline computed partition table, without unplanned interruption from other applications. Although the partition tables can be manually constructed, this can lead to poor and possibly

unschedulable solutions. We have shown in [15, 16] the way partitioning constricts the use of the processor and we proposed two optimization strategies. Thus, partitioning ensures consistent execution, and that the controller will process all the acquired spectra.

7. CONCLUSIONS

Partitioned architectures allow the safe integration of applications of different criticality levels, such as mission critical (e.g., power management, thermal control system) and scientifically critical (i.e., scientific instruments) on the same platform. Partitioning not only allows sharing the high performance computation resources, but also reduces the complexity and cost of system development and integration. In this paper we developed a controller for a rugged rotary Fourier Transform Infrared Spectrometer on a FPGA and a real-time processor. We evaluated the SNR performance impact of implementing the controller on a partitioned architecture.

REFERENCES

- [1] V. Saptari, "Fourier-Transform Spectroscopy Instrumentation Engineering", SPIE Press, 2004.
- [2] J. Rushby. "Partitioning for avionics architectures: Requirements, mechanisms, and assurance". NASA Contractor Report CR-1999-209347, NASA Langley Research Center, June 1999
- [3] J. Windsor and K. Hjortnaes, "Time and Space Partitioning in Spacecraft Avionics", Third IEEE International Conference on Space Mission Challenges for Information Technology, 2009.
- [4] Gronholz, Joern, and Werner Herres. "Understanding FT-IR data processing. Part 2: details of the spectrum calculation." *Instruments and Computers (Reprint)* 3 (1985).
- [5] W. Wadsworth and J. Dybwad, "Rugged high-speed rotary imaging Fourier transform spectrometer for industrial use", Proc. SPIE, Vol. 4577, No. 83, 2002, pp 83–88.
- [6] D.F. Berisford et al, "Thermal testing of the compositional infrared imaging spectrometer (CIRIS)", Proc of the International Conference on Environmental Systems, 2012.
- [7] V. Formisano et al, "The Planetary Fourier Spectrometer (FPS) on board of the European Mars Express Mission", Planetary and Space Science, Vol. 53, 2005, pp-963–974.
- [8] M. Anderson et al, "Fourier transform infrared spectroscopy for Mars science", Review of Scientific Instruments, Vol. 76, 2005.
- [9] National Instruments "NI CompactRIO – Reconfigurable Control and Acquisition System", white paper
- [10] S. Uruena et al. "A new approach to memory partitioning in on-board spacecraft software". Proceedings of the Reliable Software Technologies – Ada Europe, 2008
- [11] J.Windsor et al., "Integrated Modular Avionics for Spacecraft – User requirements, architecture and role definition", Proceedings of Digital Avionics Systems Conference, 2011
- [12] G. Horvath et al., "Safety-critical partitioned software architecture: a partitioned software architecture for robotic spacecraft", Proceedings of the Aerospace Conference, 2011
- [13] J. Windsor et al., "Time and Space partitioning security components for spacecraft flight software", Proceedings of Digital Avionics Systems Conference, 2011
- [14] A. Ebel et al., "Effects of zero-filling and apodization on spectral

integrals in discrete Fourier-transform spectroscopy of noisy data”, Journal of Magnetic Resonance, Vol. 182, 2006, pp-330—338

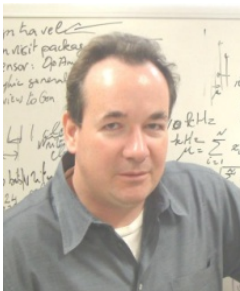
- [15] D. Tamas-Selicean and Paul Pop, “Optimization of Time-Partitions for Mixed-Criticality Real-Time Distributed Embedded Systems”, Proceedings of the International Symposium on Object/Component/Service-Oriented Real-Time Distributed Computing Workshops, 2011.
- [16] D. Tamas-Selicean and Paul Pop, “Design Optimization of Mixed-Criticality Real-Time Applications on Cost-Constrained Partitioned Architectures”, Proceedings of the Real-Time Systems Symposium, 2011.
- [17] FAULHABER Series E2 Optical Incremental Encoders datasheet:http://www.micromo.com/datasheets/Encoders/E2_MME.pdf
- [18] L. Mertz. “Auxiliary computation for Fourier spectroscopy”, Infrared Physics, Vol. 7, 1967, pp-17—23, Pergamon Press

BIOGRAPHY



Domițian Tămaș-Selicean is a PhD student at DTU Compute, Technical University of Denmark (DTU). He received his Dipl. Ing. degree in Computer Engineering from the “Politehnica” University of Timisoara. He is doing research in the area of system-level design of mixed-criticality embedded systems and is expected to finish his doctoral studies in November 2013. In 2012 he was a visiting scholar for 5 months at the Jet Propulsion

Laboratory. Prior to his PhD studies, he worked as a software developer.



Didier Keymeulen received the BSEE, MSEE and Ph.D. in Electrical Engineering and Computer Science from the Free University of Brussels, Belgium in 1994. In 1996 he joined the computer science division of the Japanese National Electrotechnical Laboratory as senior researcher. Currently he is principal member of the technical staff of JPL in the Bio-Inspired Technologies Group. At JPL,

he is responsible for DoD and NASA applications on evolvable hardware for adaptive computing that leads to the development of fault-tolerant electronics and autonomous and adaptive sensor technology. He participated also as test electronics lead, to Tunable Laser Spectrum instrument on Mars Science Laboratory. He served as the chair, co-chair, and program-chair of the NASA/ESA Conference on Adaptive Hardware. Didier is a member of the IEEE.



Daniel F. Berisford received the B.S. degree in aerospace engineering from the Georgia Institute of Technology in 2002, and the M.S. and PhD degrees in aerospace engineering from The University of Texas at Austin in 2004 and 2009. His graduate research included the development of optical and thermal diagnostic instruments for electromagnetic railguns and plasma

thrusters. Dr. Berisford is currently a member of the technical staff at the Jet Propulsion Laboratory in Pasadena, CA, where he performs research and development work for advanced spacecraft thermal technologies and optical instruments for icy worlds. Dr. Berisford specializes in rapid experiment development to address fundamental engineering challenges of emerging technology in thermal, fluid, and optical systems.



Robert Carlson obtained his PhD in Physics from the University of Southern California and is a Senior Research Scientist at JPL. He does planetary spectroscopy using spacecraft, Antarctic field measurements, and laboratory measurements. He was Principal Investigator for the Galileo Near Infrared Mapping Spectrometer (NIMS) and is a Co-Investigator on ESA’s Venus Express and Rosetta Visible and Infrared Imaging Spectrometers (VIRTIS). His laboratory work concentrates on the radiolysis and photolysis of cosmic and planetary ices and cloud condensates. Carlson is the past Editor of the Journal of Geophysical Research.



Kevin P. Hand is Deputy Chief Scientist for Solar System Exploration at JPL. His research focuses on the origin, evolution, and distribution of life in the solar system with an emphasis on moons of the outer solar system that likely harbor liquid water oceans. Dr. Hand earned a Bachelors in physics and astronomy from Dartmouth College, a Masters in Mechanical Engineering from Stanford

University, and a PhD from Stanford’s Department of Geological & Environmental Sciences.



Prof. Paul Pop is an Associate Professor at DTU Compute, Technical University of Denmark (DTU). He has received his Ph.D. degree in computer systems from Linköping University in 2003. His main research interests are in the area of system-level design of embedded systems. He has published extensively in this area, and has received the best paper award at the Design, Automation and Test in

Europe Conference (DATE 2005) at the International Conference on Compilers, Architecture, and Synthesis for Embedded Systems (CASES 2010). His research has been highlighted as “The Most Influential Papers of 10 Years DATE”. He has served on the technical program committee of numerous conferences, such as DATE, ICCAD, CODES+ISSS and RTSS. At DTU Compute, he is the coordinator of a research group focusing on safety-critical embedded systems, with a focus on mixed-criticality systems. He participates in several national and EU projects in this area.



Winthrop Wadsworth: *B.S. Rensselaer Polytechnic Institute 1976, M. Eng Cornell University 1977, Control Optics Corp. 1977-1980, Perkin-Elmer Corp. 1980-1984, Consultant 1984-1991, Designs & Prototypes, Ltd. 1991-present.*

Technology under a contract with the National Aeronautics and Space Administration during Domițian Tămaș-Selicean's research stay. The research stay of Domițian Tămaș-Selicean was made possible with financial support from the Technical University of Denmark, Oticon Fonden and Otto Mønstedts Fond and the hospitality of the Jet Propulsion Laboratory, California Institute of Technology.



Ralph Levy: *A.B., Sc.B. Brown University, M.S. University of Pennsylvania / The Wharton School. Mr. Levy is CTO at Quant Engineering. Many of the products under development have critical safety and dependability aspects, where people's safety depends on the reliability of the product. Mr. Levy is responsible for the technical development and growth of personnel*

and for the scientific integrity of the products and services provided by Quant Engineering.

APPENDIX A: RUNNING SIGNAL-TO-NOISE RATIO (SNR)

SNR measures “the ability to reproduce the spectrum from the same sample and the same conditions” [1]. We compute the SNR according to the formulas presented [1]:

$$SNR = \frac{1}{N_{rms}} \quad (9)$$

using the root-mean-square N_{rms} of the spectral noise $N(v)$:

$$N_{rms} = \sqrt{\frac{1}{n} \sum_{i=1}^n [N(v_i)]^2} \quad (10)$$

where n is the number of wavelengths in the spectrum. The spectral noise between two spectra T_a and T_b of the same sample measured at different times is computed according to the following equation:

$$N(v) = 1 - \frac{T_a(v)}{T_b(v)} \quad (11)$$

With the running SNR, we compute the SNR over an interval of a given number of points of the two output spectra. We shift this interval one point at the time, to cover the whole spectral interval.

ACKNOWLEDGEMENTS

The research described in this paper was carried out at the Jet Propulsion Laboratory, California Institute of